Contents lists available at ScienceDirect

Bioactive Materials

2-N, 6-O sulfated chitosan evokes periosteal stem cells for bone regeneration

Luli Ji [a,c], Yuanman Yu [a,c], Fuwei Zhu [a,c], Dongao Huang [a,c], Xiaogang Wang [a,c,**], Jing Wang [a,b,*], Changsheng Liu [a,c,d,***]

[a] *Key Laboratory for Ultrafine Materials of Ministry of Education, East China University of Science and Technology, Shanghai, 200237, PR China*
[b] *The State Key Laboratory of Bioreactor Engineering, East China University of Science and Technology, Shanghai, 200237, PR China*
[c] *Engineering Research Center for Biomedical Materials of the Ministry of Education, East China University of Science and Technology, Shanghai, 200237, PR China*
[d] *Frontiers Science Center for Materiobiology and Dynamic Chemistry, East China University of Science and Technology, Shanghai, 200237, PR China*

ARTICLE INFO

ABSTRACT

Musculoskeletal injuries and bone defects represent a significant clinical challenge, necessitating innovative approaches for effective bone tissue regeneration. In this study, we investigated the potential of harnessing periosteal stem cells (PSCs) and glycosaminoglycan (GAG)-mimicking materials for *in situ* bone regeneration. Our findings demonstrated that the introduction of 2-N, 6-O sulfated chitosan (26SCS), a GAG-like polysaccharide, enriched PSCs and promoted robust osteogenesis at the defect area. Mechanistically, 26SCS amplifies the biological effect of endogenous platelet-derived growth factor-BB (PDGF-BB) through enhancing the interaction between PDGF-BB and its receptor PDGFRβ abundantly expressed on PSCs, resulting in strengthened PSC proliferation and osteogenic differentiation. As a result, 26SCS effectively improved bone defect repair, even in an osteoporotic mouse model with lowered PDGF-BB level and diminished regenerative potential. Our findings suggested the significant potential of GAG-like biomaterials in regulating PSC behavior, which holds great promise for addressing osteoporotic bone defect repair in future applications.

1. Introduction

Musculoskeletal injuries caused by aging, disease, sports and traffic accidents are dramatically increasing these years. Regeneration of defect site can be achieved through *ex vivo* bone tissue engineering or *in situ* bone regeneration [1]. Conventional *ex vivo* bone tissue engineering composed of biomaterial scaffold, patient-derived cells and biological factors has notable limitations, including the lack of reliable cell sources, complex culture conditions, the high price of bioactive factors, and poor homing and engraftment efficacy. To avoid such drawbacks, targeting endogenous skeletal stem cells for *in situ* bone regeneration could be an alternative therapy [2,3], which utilizes the body's innate regenerative potential without the assistance of exogenous cells [4,5]. Biomaterials

for *in situ* tissue repair, in addition to serving as a structural framework [6], requires precise coordination of biophysical and biochemical cues to induce host progenitor or stem cells to the defect site and direct cells to differentiate in a controlled way [7].

Periosteum, a reservoir of endogenous cytokines and stem cells at the exterior surface of cortical bone, possesses potent regenerative potential for skeletal osteogenesis [8–10]. It has been reported that a periosteal stem cell (PSC) is present in the periosteal mesenchyme, which displays clonal multipotency and self-renewal, and sits at the apex of a differentiation hierarchy [11]. Distinct from bone marrow mesenchymal stem cells (BMSCs) which mediate endochondral ossification, PSCs form bone *in vivo* via intramembranous ossification. Nevertheless, PSCs acquire endochondral bone formation capacity in response to injury and

contribute to trabecular formation in the defect area [11,12]. In a recent study comparing the regenerative potential of periosteum-derived cells and BMSCs, the results showed higher regenerative capacity and increased contribution of PSCs in fracture repair [13]. According to the latest report, periosteal stem cells play a controlling role in regulating growth plate stem cells and DDR2$^+$ calvarial stem cells respectively during postnatal skeletal growth and calvarial suture fusion, suggesting its position of leadership in stem cell-involved bone development [14,15]. Some studies have combined exogenous BMSCs [16,17] or periosteum-derived progenitor cells [18–20] with biomaterials for bone repair. However, the contribution of host periosteal stem cells has hardly been explored in biomaterial-mediated *in situ* bone regeneration. Moreover, under pathological situations like osteoporosis and aging, endogenous PSCs face the exhaustion of both quality and quantity [21], which might result in bone repair failure. To solve this problem, explorations on utilizing the biological effect of biomaterials to regulate PSCs and bring their regenerative potential into full play is in great anticipation.

PSCs reside in extracellular matrix (ECM) rich in glycosaminoglycans (GAGs). GAGs are linear polysaccharides present on the cell surface, in the intracellular milieu, and in extracellular matrix [22], which are known to regulate cell behaviors by interacting with GAG-binding proteins and mediating cell signal pathways [23,24]. However, GAGs are hardly applied in practical use due to the heterogeneity of their chemical structures [23,25]. The fabrication of GAG-mimicking materials with defined and controllable structures as substitutes for natural GAGs is of great significance. Our previous studies have confirmed the interaction between a GAG-like sulfated chitosan (2-N, 6-O sulfated chitosan, 26SCS) and exogenous proteins like recombinant human bone morphogenetic protein-2 (rhBMP-2) [26]. In this study, we attempt to explore the coordination of 26SCS with endogenous cytokines or growth factors and the regulatory effect on host PSCs to realize *in situ* bone regeneration.

To this end, we introduced 26SCS into bone defect area and investigated the spatiotemporal pattern of endogenous cytokines and the responsive PSCs. We observed an enrichment of PSCs and platelet-derived growth factor-BB (PDGF-BB) in 26SCS treated group at the early stage. Subsequently, the recruited PSCs differentiated into Osterix$^+$ osteoblasts and contributed to osteogenesis at the defect site, coupled with type H vessel formation. Mechanistically, 26SCS could bind to PDGF-BB, strengthen the combination of PDGF-BB to its receptor PDGFRβ and upregulate PDGFRβ phosphorylation, thus promoting PSC proliferation and osteogenic differentiation. Notably, 26SCS could amplify the biological effect of endogenous PDGF-BB even when its initial level was relatively lower in osteoporotic mouse bone defect model. Our findings suggested that 26SCS was able to evoke PSC-mediated *in situ* bone regeneration through the capture and amplification of endogenous PDGF-BB and provided a material-based PSC-dominated strategy for bone tissue repair.

2. Results

2.1. 26SCS/GelMA scaffold promotes mouse bone defect healing

Gelatin Methacryloyl (GelMA) is an olefin double bond modified gelatin that can be quickly cured into a gel through UV and visible light under the action of photo-initiators. GelMA hydrogel has good biocompatibility and mechanical properties with a three-dimensional structure, which is suitable for cell growth and differentiation [27]. Besides, the mechanical strength of GelMA hydrogel can be adjusted by different GelMA concentrations. In this study, we prepared 5 %, 10 % and 15 % GelMA scaffolds and determined their mechanical strength. The results showed that the elastic modulus was gradually increased with the increase of GelMA concentration, which was 18.75 kPa (5 %), 39.21 kPa (10 %), and 102.7 kPa (15 %), respectively (Fig. S1A). However, the fragility of the scaffolds was also increased when the

GelMA concentration was upregulated, which was unfavorable for maintaining the mechanical microenvironment. It has been reported that substrates approximating to the elastic moduli of brain (0.1–1 kPa), muscle (8–17 kPa) and collagenous bone (25–40 kPa) direct stem cells to commit to neurocytes, myoblasts and osteoblasts, respectively. Taken together, we selected 10 % GelMA for further experiments. 26SCS was pre-mixed into GelMA solution to prepare 26SCS/GelMA scaffolds. The morphologies of GelMA and 26SCS/GelMA scaffolds were observed by scanning electron microscopy (SEM). The images exhibited the porous structure of both scaffolds and the successful load of 26SCS on the scaffold (Fig. 1B). Fourier transform infrared spectroscopy (FTIR) analysis of both GelMA and 26SCS/GelMA scaffolds showed peaks at 1630, 1535, and 1240 cm^{-1} related to the C=O stretching (amide I), N–H bending (amide II), and C–N stretching plus N–H bending (amide III), respectively. Moreover, an N–H stretching (amide A) and –OH stretching vibration peak could be observed at 3270 cm^{-1}, with a C–H bending peak at 1450 cm^{-1}. These peaks corresponded to GelMA characteristic functional groups. The load of 26SCS on the GelMA scaffold was further confirmed by the stretching vibrations of O=S=O and C–O–S groups respectively at 1230 cm^{-1} and 810 cm^{-1} in FTIR spectra of 26SCS/GelMA scaffold (Fig. 1C). We then evaluated the release kinetics of 26SCS from the scaffold. The results showed a burst release of 26SCS at the initial stage and remained a stable liberation in the subsequent process (Fig. S1B). To examine the biological property of the scaffolds, we cultured C2C12 cells on the surface of the scaffolds and found that both scaffolds were suitable for cell adhesion (Fig. S1C). In addition, 26SCS/GelMA extracted medium had no obvious cell cytotoxicity (Fig. S1D). To further investigate the *in vivo* biocompatibility, scaffolds were subcutaneously implanted into the back skin of mice. After 14 days, the implants were taken out for immunohistochemical analysis. As shown in F4/80 immunohistochemical staining images, although there were inflammatory cells distributing around the implants, they did not invade the interior of the implants (Fig. S1E). These results confirmed the good biocompatibility of GelMA and 26SCS/GelMA scaffolds.

To explore the effect of 26SCS on bone regeneration, we first implanted 26SCS/GelMA or, as a control, blank GelMA into the defect area of mouse femur (Fig. 1A). At week 8 post-surgery, the femurs were harvested and analyzed by Micro-computed tomography (Micro-CT). The results showed substantially larger amount of new bone formation in 26SCS/GelMA implanted femur, as compared to the controls (Fig. 1D). The ratio of high-density bone volume to tissue volume (BV/TV) and thickness of trabecular (Tb.Th) in 26SCS/GelMA group are respectively nearly 2.1-fold and 3.3-fold higher than that in control group (Fig. 1E and F). Additionally, hematoxylin and eosin (H&E) staining and Masson staining results confirmed significantly more newly formed trabecula bone in the defect area of 26SCS/GelMA group, as compared to that of the controls (Fig. 1G and H). Calcein double staining results also exhibited more bone formation in 26SCS/GelMA group (Fig. 1I–K). The level of osteocalcin (OCN), a marker of osteogenic activity, was examined in the supernatant of ground bone defect tissue, which was significantly upregulated in 26SCS/GelMA group (Fig. 1L), indicating increased osteogenic activity. Taken together, these results suggested that 26SCS/GelMA could significantly promote bone regeneration in the defect area.

2.2. 26SCS/GelMA promotes PSC recruitment and osteogenic differentiation at the defect site

Periosteum-derived stem cells have been proved to be very important for bone modeling and remodeling. PSCs are expected to rapidly respond to bone injury signals and get involved in the repair process. We analyzed the implants via immunofluorescence staining at earlier stage of bone healing. At week 2 post-surgery, the number of CD200$^+$CTSK$^+$ PSCs in 26SCS/GelMA implanted defect was significantly higher than that in control group (Fig. 2, A and C). To investigate PSC-mediated
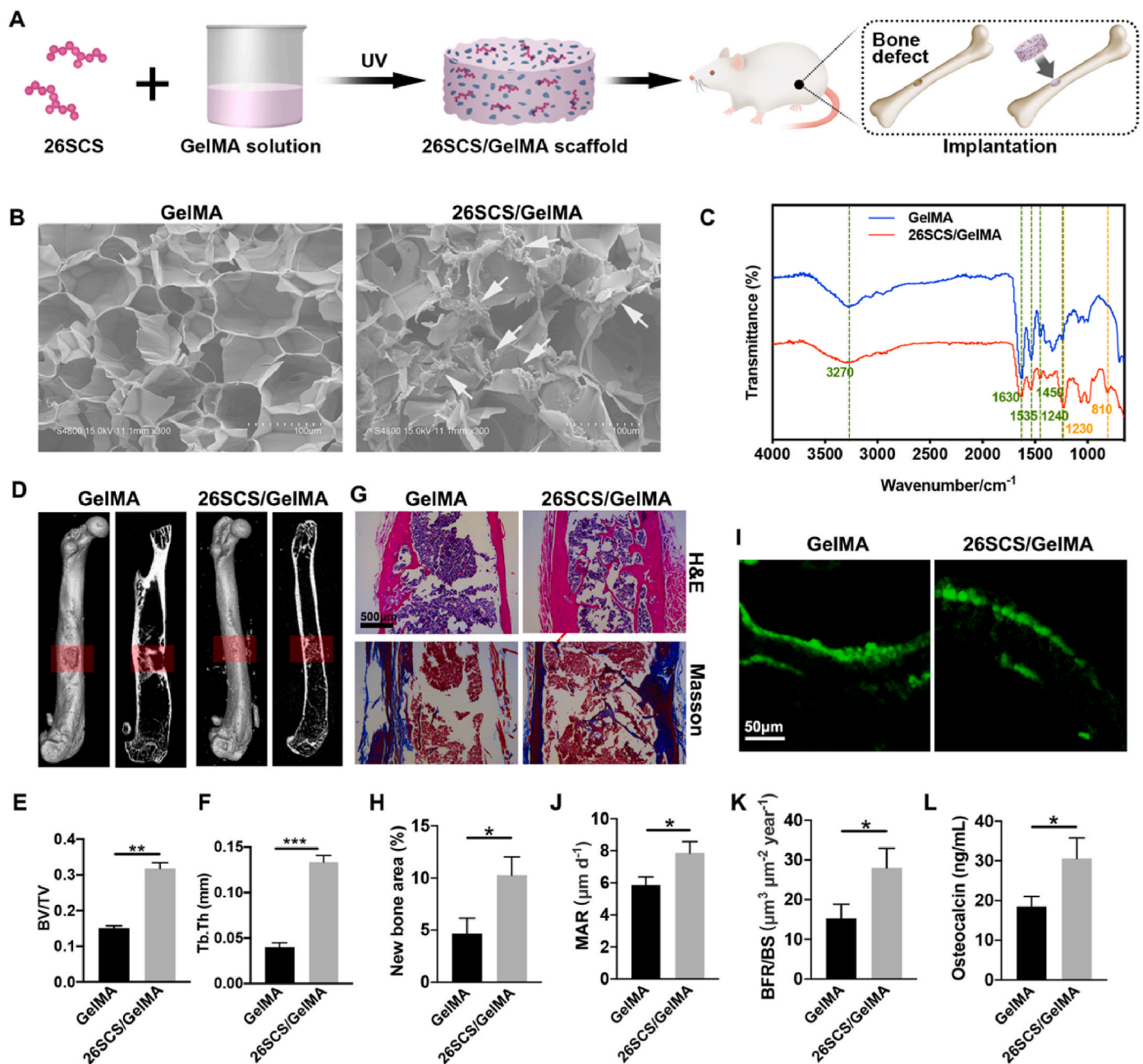
Fig. 1. 26SCS/GelMA scaffold promotes new bone formation at the defect area of mouse femur. (A) Illustration of mouse femur defect model. (B) Scanning electron microscopy micrographs of GelMA and 26SCS/GelMA scaffolds. White arrows, coated 26SCS. (C) FTIR-ATR characterization of GelMA and 26SCS/GelMA scaffolds. (D) Representative micro-CT images of mouse femora implanted with GelMA scaffold and 26SCS/GelMA scaffold at week 8 post-surgery. (E and F) Quantitative measurements of trabecular bone fraction (BV/TV) and trabecular thickness (Tb. Th). (G) Representative images of H&E staining and Masson staining of mouse femora from GelMA and 26SCS/GelMA groups respectively. (H) Quantitative analysis of new bone area at the defect site at week 8 post-surgery. (I–K) Representative confocal images of calcein double labeling of defect area with quantification of mineral apposition rate (MAR) and bone formation rate (BFR). (L) Osteocalcin concentration at the defect area by ELISA. Data shown as mean $\pm$ s.d. $*P < 0.05$, $**P < 0.01$, $***P < 0.001$ ($n = 3$ per group).

osteogenesis at the defect area, the samples were harvested and stained with CD200 and osteoblast marker Osterix at week 4 post-surgery. Significantly larger double positive area was observed in 26SCS/GelMA group (Fig. 2, B and D), indicating more PSC-derived osteoblasts in the process of reconstructing the defect area, as compared to the controls. Periostin has been reported to be a novel marker for intramembranous ossification [28–30] and associated with enhanced response to injury of periosteal cells [13]. 26SCS/GelMA significantly upregulated periostin level in the defect area (Fig. 2E and F), suggesting that 26SCS induced an improved osteogenic microenvironment after bone injury.

To investigate the temporally changing trend of PSC abundance in the defect area, the samples were digested enzymatically and analyzed by flow cytometry at day 3, 7, 14 and 28 post-surgery, respectively (Fig. 2G, Fig. S2). The data revealed that the number of PSCs increased with time and reached its maximum at day 14, followed by a decline at day 28 (Fig. 2H). Meanwhile, the number of PSCs at the defect in 26SCS/GelMA group was significantly larger at all time points, especially at day 14, which was nearly 3 times larger than that in control group (Fig. 2H). The above results suggested that 26SCS recruited a large number of PSCs to the defect area at the early stage of bone healing and provided a preferable osteogenic microenvironment for new bone formation.
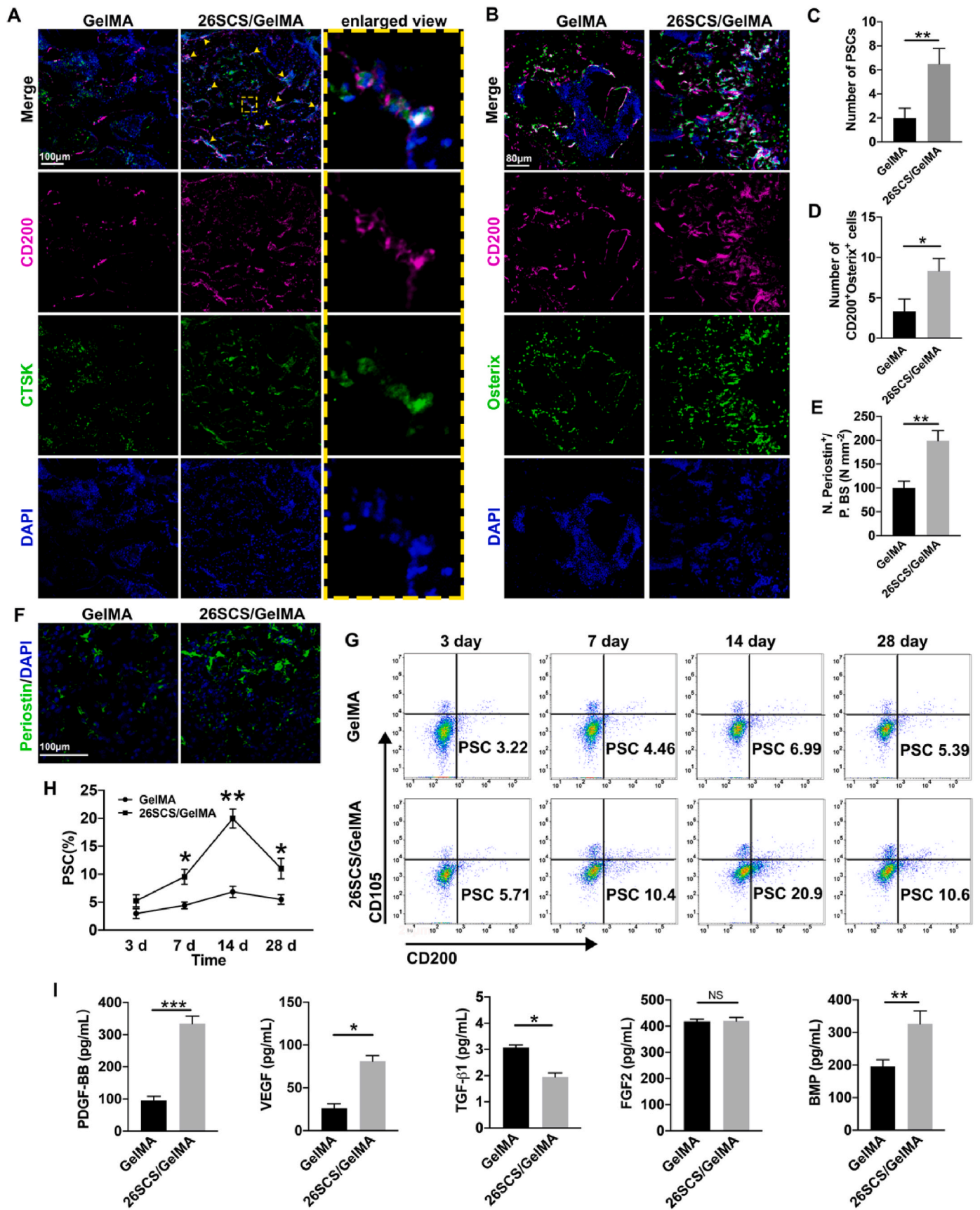
(caption on next page)

Fig. 2. 26SCS/GelMA promotes the enrichment of PSCs and various growth factors at the defect site. (A) Representative confocal images of immunostaining of CD200 (purple), and CTSK (green) and DAPI (blue) staining of nuclei in the defect area of mouse femora at week 2 post-surgery. (B) Representative confocal images of immunostaining of CD200 (purple), and Osterix (green) and DAPI (blue) staining of nuclei in the defect area of mouse femora at week 4 post-surgery. (C) Quantitative analysis of the number of CD200+CTSK+ periosteal stem cells. (D) Quantitative analysis of the number of CD200+Osterix+ osteoblasts derived from PSCs. (E and F) Representative confocal images of immunostaining of Periostin (green) and DAPI (blue), and quantitative analysis of periostin level at the defect area at week 4 post-surgery. (G and H) Flow cytometry analysis of the percentage of PSCs at the defect area from Day 3 to Day 28 post-surgery. (I) The concentrations of growth factors at the defect area measured by ELISA at week 2 post-surgery. White arrowheads, double-positive area; white dashed lines, defect area. Data shown as mean ± s.d. *$P < 0.05$, **$P < 0.01$, ***$P < 0.001$ ($n = 3$ per group).

Endogenous cytokines and growth factors are secreted after the injury stimulus, to recruit mesenchymal stem cells and promote bone healing [31,32]. We quantified the expression levels of various growth factors in the defect area at week 2 post-surgery, including PDGF-BB, vascular endothelial growth factor (VEGF), transforming growth factor-β1 (TGF-β1), fibroblast growth factor-2 (FGF-2), and BMP-2 and found that the expressions of PDGF-BB, VEGF, and BMP-2 in 26SCS/GelMA group were significantly higher than that in the control group (Fig. 2I). According to Cao Xu et al., PDGF-BB secreted by

tartrate-resistant acid phosphatase positive (TRAP+) mononuclear cells could induce the recruitment of periosteum-derived cells and maintain periosteal bone formation and regeneration [33].

In addition, PDGF-BB and VEGF are typical angiogenic growth factors that can induce vascularization in bone, coupled with new bone formation. The immunofluorescence staining images confirmed upregulated PDGF-BB and VEGF expressions at the defect in 26SCS/GelMA group, as compared to the controls (Fig. S3A). After the implantation of scaffolds for two weeks, we analyzed the angiogenesis at the defect. It
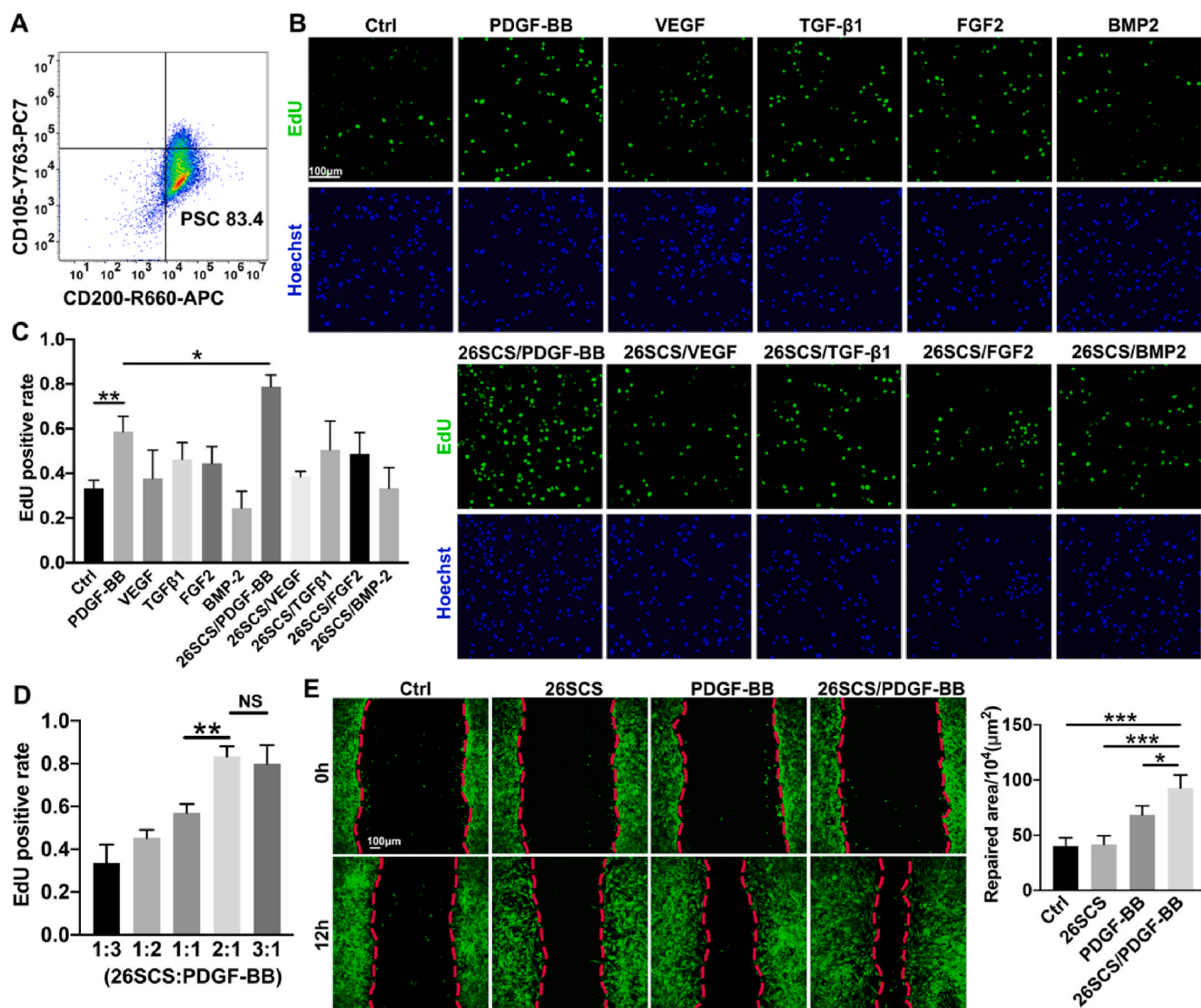

Fig. 3. 26SCS synergistically with PDGF-BB promotes PSC proliferation and migration with the optimal stoichiometry of 2:1 *in vitro*. (A) Flow cytometry analysis of isolated periosteal stem cells. (B) EdU assay of PSCs treated with 26SCS and growth factors. (C) The quantification of EdU positive nuclei (Alexa Fluor 488 azide labeled; green) and 1 × Hoechst-stained nuclei of all the cells (blue). (D) The quantification of EdU positive rate in PSCs treated with different stoichiometric ratio of 26SCS: PDGF-BB. (E) Representative wound closure assay images and quantitative analysis of repaired area of PSCs under the treatment with 26SCS and PDGF-BB. Data shown as mean ± s.d. *$P < 0.05$, **$P < 0.01$, ***$P < 0.001$; NS, not significant ($n = 3$ per group).

has been reported that type H vessels, identified with CD31^{hi}Emcn^{hi}, can strongly induce osteogenesis partially through its high throughput oxygen and material transport capacity [34]. The immunofluorescence results indicated that 26SCS/GelMA scaffold could efficiently stimulate the formation of type H vessels and α-SMA$^+$ arteries (Fig. S3, B and C). Flow cytometry analysis further confirmed significantly increased number of CD31^{hi}Emcn^{hi} endothelium of defect area in 26SCS/GelMA group compared with the control group (Fig. S3, D and E). The transcription levels of angiogenesis-related cytokines were also significantly increased, confirming the improved local angiogenesis microenvironment induced by 26SCS/GelMA scaffold (Fig. S3F). These results indicated 26SCS/GelMA potentially induced revascularization in bone defect area which effectively contributed to bone regeneration.

2.3. 26SCS synergistically with PDGF-BB promotes PSC proliferation via PDGFRβ-PI3K-AKT signaling

To explore the mechanism whereby 26SCS regulates PSC behavior in coordination with growth factors, the cells were isolated from the periosteum of mouse femora and identified via flow cytometry analysis with approximately 85 % purity for further *in vitro* experiments (Fig. 3A). We performed EdU assay of PSCs to examine the effect of
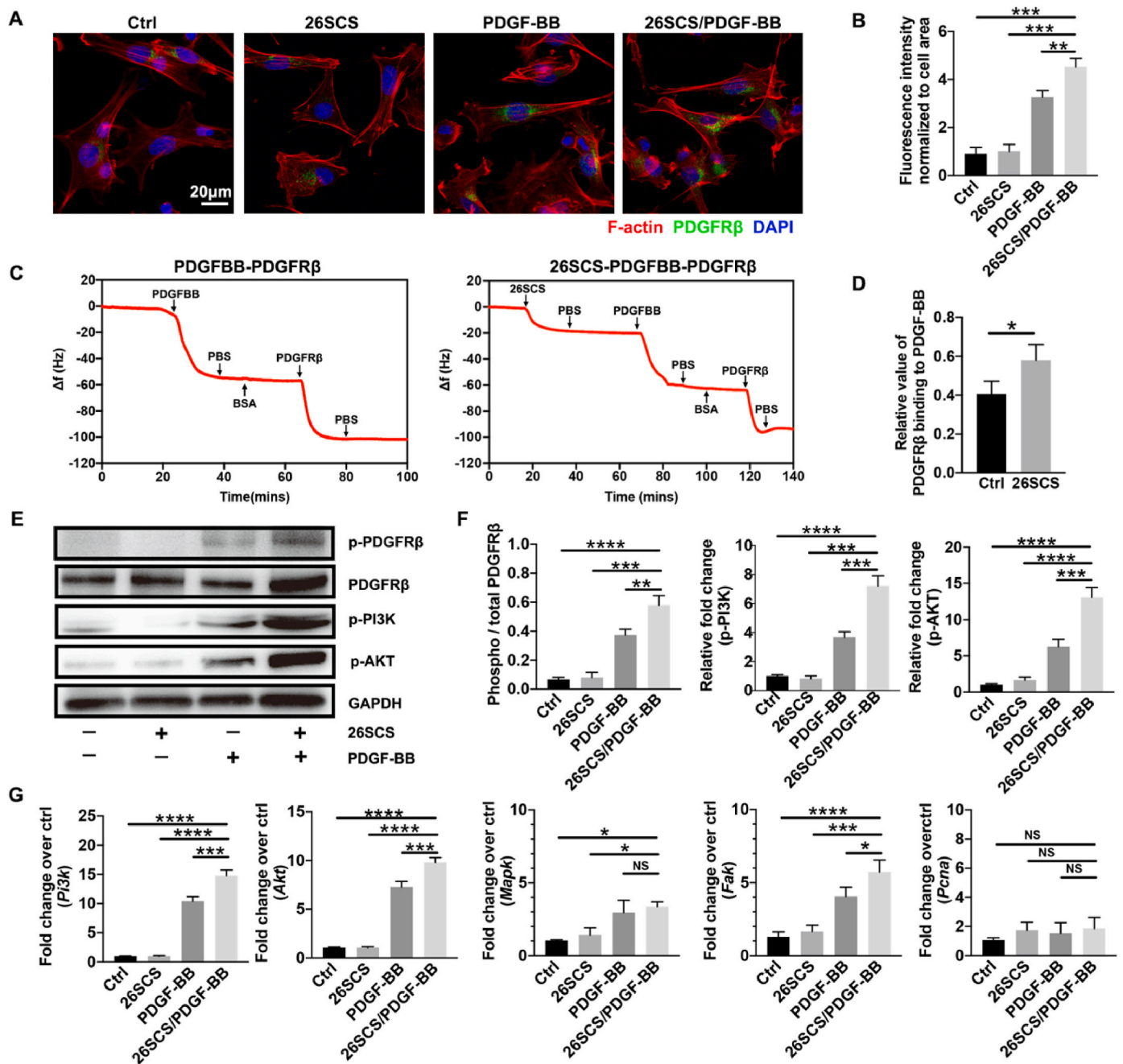

Fig. 4. 26SCS synergistically with PDGF-BB induces PDGFRβ phosphorylation and activates PI3K-AKT signaling pathway. (A) Representative confocal images of immunostaining of PDGFRβ (green), and F-actin (red) staining of cytoskeleton and DAPI (blue) staining of nuclei of PSCs under the treatment with 26SCS and PDGF-BB. (B) Quantitative analysis of PDGFRβ fluorescence intensity in different groups. (C) The binding curve of PDGF-BB and PDGFRβ under the treatment with 26SCS. (D) Quantitative analysis of relative value of PDGFRβ binding to PDGF-BB. (E and F) Western blot analysis and the quantitation of the relative level of phosphorylated PDGFRβ, PI3K, and AKT in PSCs after treating with 26SCS and PDGF-BB for 15 min. (G) Relative gene expressions of PSCs treated with 26SCS and PDGF-BB *in vitro*. Data shown as mean ± s.d. *$P < 0.05$, **$P < 0.01$, ***$P < 0.001$; NS, not significant ($n = 3$ per group).

26SCS and growth factors on PSC proliferation *in vitro*. Significantly more EdU positive cells were observed in PDGF-BB group compared with the control and other factor treatment groups (Fig. 3B and C), indicating that PDGF-BB contributed to the PSC enrichment at the defect site. Notably, 26SCS treatment amplified such effect of PDGF-BB and greatly promoted PSC proliferation, which was not obvious with other

factors (Fig. 3B and C). To determine the optimal stoichiometric ratio of 26SCS: PDGF-BB for PSC proliferation, the cells were treated with 26SCS and PDGF-BB of 1:3, 1:2, 1:1, 2:1, and 3:1 stoichiometry, respectively. The EdU positive rate reached the peak when the stoichiometric ratio of 26SCS:PDGF-BB increased to 2:1 and remained stable thereafter (Fig. 3D). Therefore, the 2:1 stoichiometry of 26SCS: PDGF-BB was
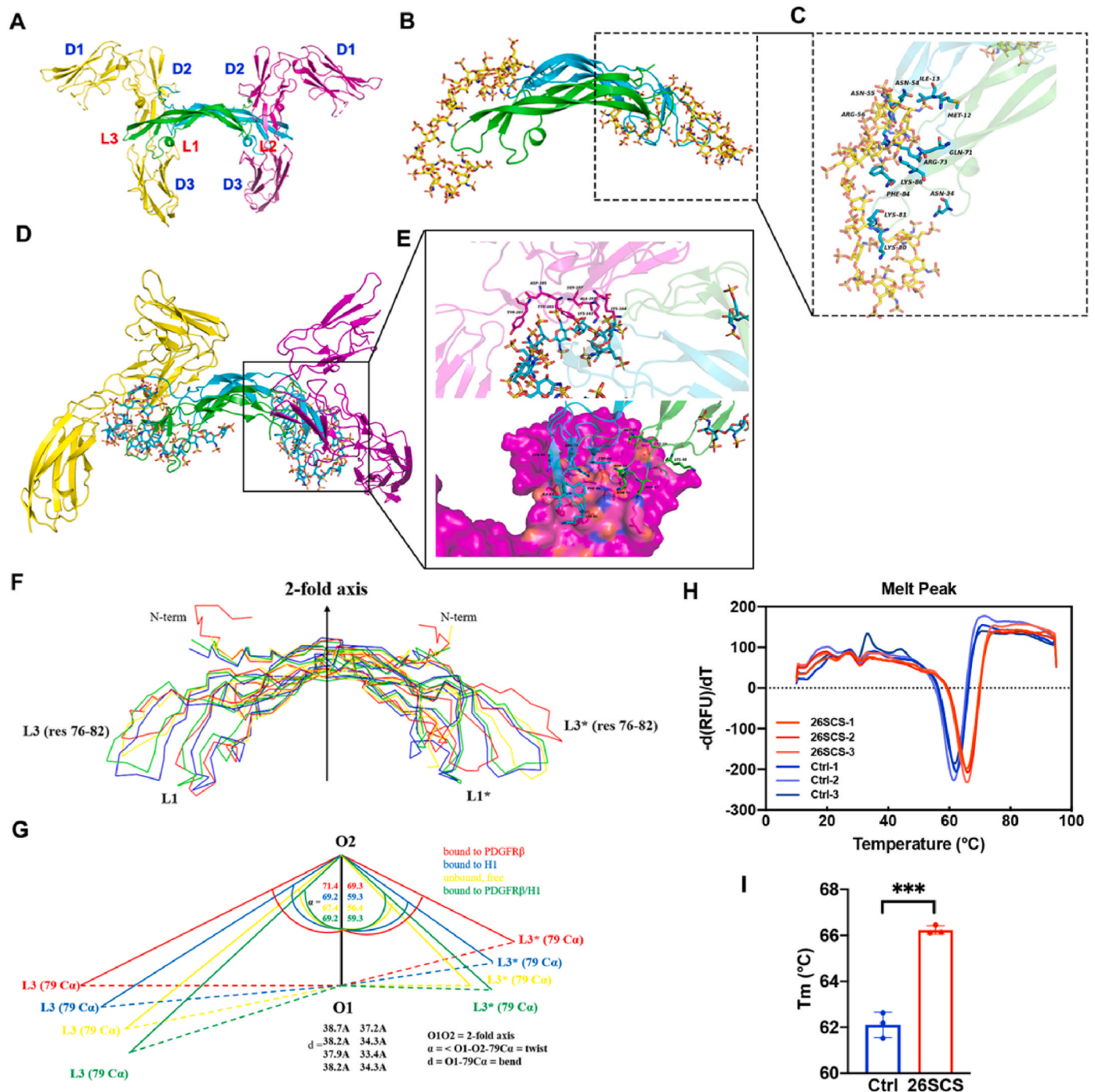

Fig. 5. 26SCS strengthens PDGF-BB-PDGFRβ binding through its combination to PDGF-BB. (A) PDGF-BB-PDGFRβ complex (PDGF-BB as green and blue, PDGFRβ as yellow and magenta). (B) 26SCS-PDGF-BB complex (26SCS shown as stick). (C) PDGF-BB and 26SCS interaction. (D) 26SCS-PDGF-BB-PDGFRβ complex (PDGF-BB-PDGFRβ same as Fig.5A and 26SCS shown as stick, yellow represents Chain X, magenta represents Chain Y). (E) PDGFRβ and 26SCS interaction, and PDGFRβ and PDGF-BB interaction in the 26SCS-PDGF-BB-PDGFRβ complex. (F) Cα trace diagram showing overlay of the PDGF-BB structures in the PDGFRβ bound form (red), the 26SCS bound form (blue), the free form (yellow), the PDGFRβ/26SCS bound form (green). (G) The displacement of loop 3 calculated as bend d (angstroms) and a bending angle, twist α (degree) relative to its respective positions in the other structures. H1 indicates 26SCS. The same coloring scheme is used as in (F). (H) Melt curves of PDGF-BB-PDGFRβ complex with (red) or without (blue) 26SCS. (I) The melting temperature (Tm) of PDGF-BB-PDGFRβ complex with or without 26SCS. Data shown as mean ± s.d. ***$P < 0.001$ ($n = 3$ per group).

selected for the following experiments. Consistently, cell cytotoxicity tests showed that PDGF-BB significantly promoted the proliferation of PSCs and 26SCS enhanced this effect (Fig. S4). In the cell migration assay, the repair area of PDGF-BB group was significantly larger than the control group and the largest repair area was observed in 26SCS/PDGF-BB group (Fig. 3E), confirming that PDGF-BB facilitated the survival and migration of PSCs, and these effects were enhanced by the involvement of 26SCS.

The PDGF family exert biology effect after the combination with its receptor PDGFRs. PSCs primarily expressed PDGFRβ, which has a strong affinity with PDGF-BB [35]. To evaluate the effect of 26SCS on PDGFRβ expression in PSCs, we performed fluorescence staining experiment. The images showed that there was a significant increase of PDGFRβ expression in 26SCS/PDGF-BB group compared with PDGF-BB group, suggesting the up-regulatory effect of 26SCS on PDGFRβ expression (Fig. 4A and B). Quartz crystal microbalance (QCM) measurements were further performed to examine the combination of PDGF-BB with PDGFRβ with or without the participation of 26SCS respectively. The curves illustrated effective combination between PDGF-BB and PDGFRβ, which is significantly strengthened by 26SCS treatment, indicating more PDGFRβ binding to 26SCS-PDGF-BB complex compared to PDGF-BB alone (Fig. 4C and D).

To further explore the signaling mechanisms of 26SCS in promotion of PDGF-BB-dependent PSC migration and proliferation, western blot assay was conducted. The results showed that PDGF-BB induced the phosphorylation of PDGFRβ, phosphoinositide 3-kinase (PI3K) and protein kinase B (AKT) in PSCs, which was further enhanced by 26SCS (Fig. 4E and F). We examined the downstream gene expression with known roles in cell migration and proliferation and found that 26SCS/PDGF-BB group expressed the highest levels of *Pi3k*, *Akt* and *Fak* relative to other groups. The mRNA expressions of *Mapk* and *Pcna* were not significant among groups (Fig. 4G). Taken together, 26SCS, synergistically with PDGF-BB, activated the phosphorylation of PDGFRβ and promoted PSC proliferation via PI3K/AKT signaling pathway.

2.4. 26SCS pretreatment strengthens PDGF-BB-PDGFRβ binding

We further studied the mechanism whereby 26SCS amplified the biological effect of PDGF-BB from the molecular aspect via AutoDock simulation. As is shown in the PDGF-BB-PDGFRβ complex, PDGF-BB binds to PDGFRβ mainly through D2/D3 loops (L1, L2, L3) (Fig. 5A). To explore the effect of 26SCS binding on PDGF-BB-PDGFRβ complex, we constructed 26SCS-PDGF-BB structure based on the above binding sites (Fig. 5B). The binding energy ΔG is −16.3 kcal/mol. Due to its inherent structural characteristics, 26SCS mainly binds to PDGF-BB through hydrogen and salt bridge bonds. The simulated structure showed that 26SCS forms hydrogen bonds with Met12, Ile13, Asn34, Asn54, Arg56, Gln71, Arg73, Lys80, Lys81, Phe84, Lys86 in PDGF-BB, and forms salt bridge bonds with the Arg and Lys amino acid residues (Fig. 5C, Table S2). Furthermore, 26SCS-PDGF-BB-PDGFRβ complex was constructed (Fig. 5D) and the binding sites between 26SCS-PDGF-BB and PDGFRβ were shown and listed (Fig. 5E, Tables S3–4). The binding energy of 26SCS-PDGF-BB-PDGFRβ is decreased to −107.62 kcal/mol, relative to −90.65 kcal/mol of PDGF-BB-PDGFRβ without 26SCS, indicating enhanced PDGF-BB binding to PDGFRβ after its binding to 26SCS, which might theoretically explain the observed increased PDGF-BB-PDGFRβ binding with 26SCS pretreatment in QCM assay (Fig. 4C and D). Superimposing the structure of the PDGF-BB molecule as observed in 26SCS-PDGF-BB structure (blue) onto the conformations seen in the unbound state (yellow), in bound states with PDGFRβ (red) and in 26SCS-PDGF-BB-PDGFRβ complex (green) indicated considerable displacement (bend and twist) in the PDGF-BB structure relative to one another (Fig. 5F and G). The PDGF-BB structure in 26SCS-PDGF-BB complex exhibited an increased twist angle by 4.7° and bending distance by 1.2 Å compared with free PDGF-BB (Fig. 5G). Based on above results, 26SCS binds to PDGF-BB and strengthens the protein stability at

the loop region, eliminates the negative effect of PDGF-BB loop region instability on PDGFRβ binding, thus improving the ultimate binding efficiency between 26SCS-PDGF-BB and PDGFRβ.

According to previous studies, the dimerization of growth factor receptors plays a crucial role in the activation of downstream signals [36–42]. We compared the stability of PDGF-BB-PDGFRβ dimers with or without 26SCS binding by measuring their unfolding/melting temperatures (Tm) using a fluorescence dye-based thermal shift assay. Tm of the 26SCS-PDGF-BB-PDGFRβ dimer was higher by 4.1 °C than that of PDGF-BB-PDGFRβ dimer without 26SCS (Fig. 5H and I). This suggested increased stability of PDGF-BB-PDGFRβ dimer upon 26SCS binding. Taken together, 26SCS treatment attributes to the 'flattened' PDGF-BB conformation, the enhanced PDGF-BB-PDGFRβ binding, and the stabilized 26SCS-PDGF-BB-PDGFRβ dimer, which stood a good chance of activating more PDGFRβ phosphorylation and the downstream PI3K/AKT signaling as shown in western blot results (Fig. 4E and F).

2.5. 26SCS synergistically with PDGF-BB promotes PSC osteogenic differentiation

To explore the effect of 26SCS and PDGF-BB on the multi-potent differentiation capability of PSCs, we performed *in vitro* multi-differentiation experiments. Alizarin Red, Oil Red O and Alcian Blue staining results demonstrated clonal multipotency of PSCs for differentiation into mature osteoblasts, adipocytes, and chondrocytes. Significantly more calcium nodules were observed in 26SCS/PDGF-BB group than others, indicating enhanced osteogenic differentiation driven by the treatment of 26SCS/PDGF-BB (Fig. 6A). In addition, 26SCS/PDGF-BB group showed inhibited adipogenesis compared with the control group and PDGF-BB group, consistent with the previous study that the commitment of skeletal stem cells to osteogenesis and adipogenesis is mutually exclusive [43,44]. Additionally, 26SCS along with PDGF-BB significantly upregulated osteogenesis-related genes *Runx2* and *Osterix* compared to the control group and the group treated with pure PDGF-BB. However, the treatment of PSCs with 26SCS alone didn't exhibit obvious promoting effect on *Runx2* and *Osterix*, indicating that 26SCS worked in coordination with PDGF-BB to induce osteogenesis (Fig. 6B).

We learned that 26SCS upregulated periostin expression *in vivo* (Fig. 2C). Consistently, significantly improved periostin mRNA and protein expression were observed in PSC-induced osteoblasts treated with PDGF-BB, and 26SCS further amplified this effect (Fig. 6C and D). We further elucidated the signaling mechanism of 26SCS/PDGF-BB-induced osteogenesis upregulation and found that 26SCS/PDGF-BB induced the phosphorylation of cAMP-response element binding protein (CREB), which subsequently activated Sp7 transcription factor (also known as Osterix) which is known to be crucial for osteogenesis (Fig. 6E). Taken together, 26SCS synergistically with PDGF-BB increased periostin expression and improved PSC-mediated osteogenesis via CREB/Sp7 signaling.

We further evaluated human umbilical vein endothelial cell (HUVEC) tube formation ability with the treatment of 26SCS and PDGF-BB. Consistent with improved angiogenesis at the bone defect, *in vitro* experiments showed that 26SCS synergistically with PDGF-BB promoted the tube formation of HUVECs (Fig. S5). These results confirmed that 26SCS amplified the biological effects of PDGF-BB on regulating proliferation and differentiation of PSCs, and tube formation of endothelial cells.

2.6. 26SCS promotes OVX-induced osteoporotic bone regeneration

Patients with osteoporosis often suffer from delayed bone healing due to increased osteoclastic bone resorption and decreased osteoblastic bone formation. Xie et al. in both bone marrow and peripheral blood found significantly lower PDGF-BB expression level in OVX mice than in sham mice [45]. To verify whether 26SCS could induce the
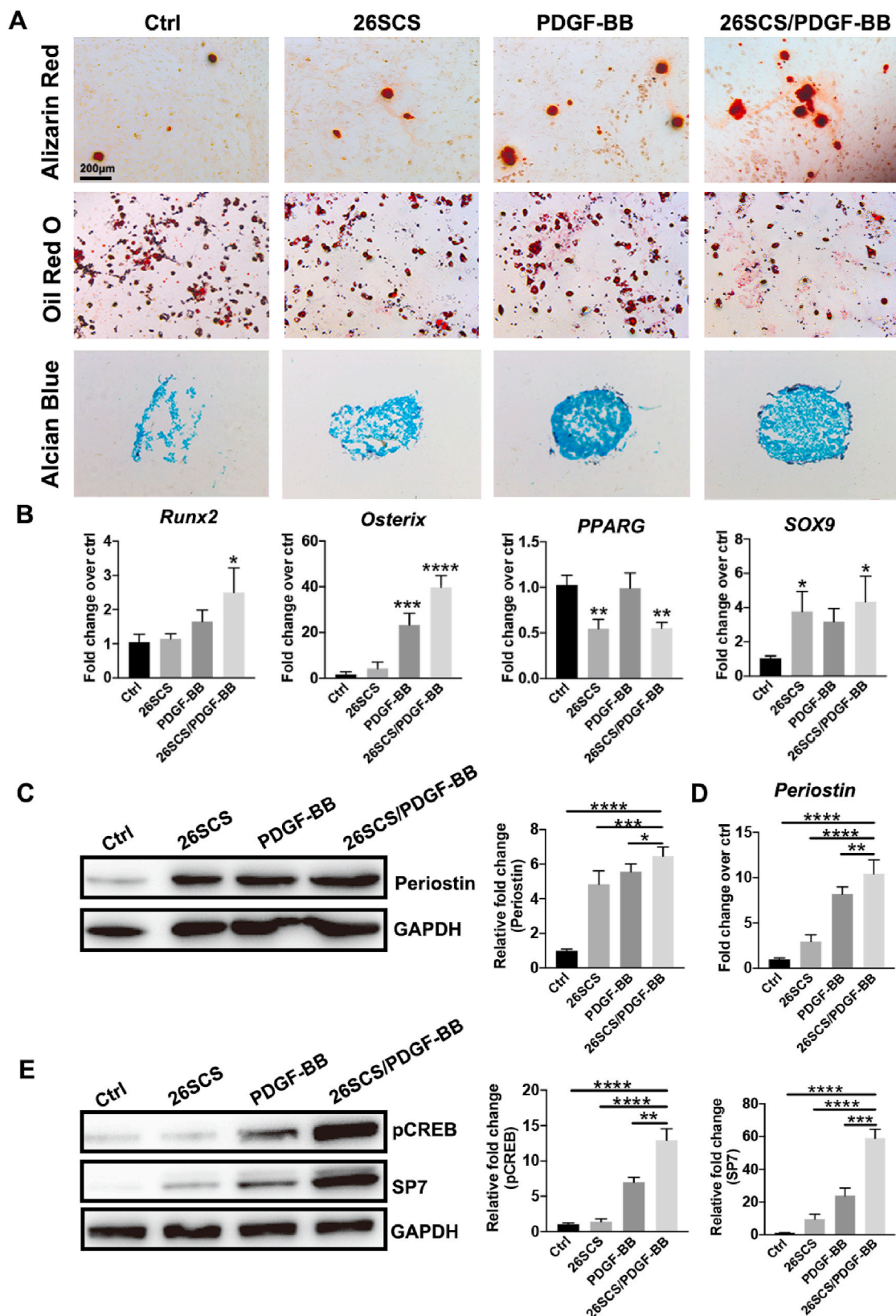
Fig. 6. 26SCS with PDGF-BB promotes PSC osteogenic differentiation and increases periostin expression. (A) Representative Alizarin Red, Oil Red O and Alcian Blue staining images of PSCs after treating with 26SCS and PDGF-BB in osteogenic differentiation medium, adipogenic differentiation medium, and chondrogenic differentiation medium, respectively. (B) Real-time PCR analysis of *Runx2*, *Osterix*, *Pparg* and *Sox9* mRNA expressions in PSCs treated with 26SCS and PDGF-BB. (C) Western blot analysis and the quantitation of the relative level of periostin in PSCs after treating with 26SCS and PDGF-BB. (D) Quantitative real-time PCR analysis of *periostin* mRNA expression in PSCs after treating with 26SCS and PDGF-BB. (E) Western blot analysis and the quantitation of the relative level of pCREB and SP7 in PSCs after treating with 26SCS and PDGF-BB. Data shown as mean ± s.d. *$P < 0.05$, **$P < 0.01$, ***$P < 0.001$, ****$P < 0.0001$; NS, not significant ($n = 3$ per group).

accumulation of PDGF-BB in osteoporosis mice, we established ovariectomy (OVX) mouse bone defect model and implanted 26SCS/GelMA, blank GelMA and PDGF-BB/GelMA (as a positive control) into the defect area. At week 2 post-surgery, the samples were collected for PDGF-BB evaluation and PSC immunofluorescence staining. The results showed the highest PDGF-BB expression level and the most $CD200^+CTSK^+$ PSCs in PDGF-BB/GelMA group. Compared to the control group, 26SCS/GelMA group exhibited significantly more PDGF-BB accumulation and PSC migration at the defect site (Fig. 7A and B), suggesting that 26SCS could upregulate PDGF-BB expression in OVX bone defect and promote the recruitment of PSCs to help with bone regeneration. At week 4, the samples were stained with OCN to investigate the distribution of mature osteoblasts. Significantly more OCN^+ osteoblasts were observed in 26SCS/GelMA and PDGF-BB/GelMA groups, suggesting the contribution of recruited PSCs to osteoblastic bone formation (Fig. 7C). The expression level of periostin which was primarily secreted by osteoblasts was elevated by 26SCS and PDGF-BB compared to the blank GelMA hydrogel (Fig. 7D). The above results suggested that 26SCS played a similar role under osteoporosis and physiologic conditions during the early stage of bone regeneration.

To evaluate bone repairment at later stage, femurs from three groups were collected for micro-CT analysis at week 8. The radiographs showed apparently more bone formation at the defect area in 26SCS/GelMA and PDGF-BB/GelMA groups, further confirmed by higher BV/TV, Tb.Th and Tb.N and lower Tb.Sp (Fig. 7E and F). Consistently, as shown by histological staining (Fig. 7G) and calcein double staining (Fig. 7H), 26SCS enhanced new bone formation and accelerated bone formation rate, as well as exogenous PDGF-BB. Interestingly, 26SCS treatment inhibited active osteoclastogenesis to a considerable extent in osteoporotic bone defect, suggesting that 26SCS might also play a role in regulating osteoclast differentiation (Fig. S6). These results verified the osteogenic effect of 26SCS *in vivo*, even in osteoporotic bone where osteogenic activity is restricted by deficient estrogen.

3. Discussion

The periosteum covers the exterior surface of cortical bone and was previously regarded as an inconspicuous bone-lining surface composed of fibroblastic cells. Recently, increasing evidence shows the presence of functionally relevant cellular heterogeneity in the periosteum [11,13, 33,35,46,47], which has been proven to play critical roles in cortical bone formation and bone fracture healing [12,33,48]. Furthermore, periosteal cells retain high growth potency and differentiation capability even in elderly patients [49]. However, the involvement of PSCs in biomaterials-mediated bone repair is often neglected. PSCs can be mediated by various biochemical signaling [50,51], whereas the mechanism under biomaterials-mediated PSC behavior remains obscure.

Significantly upregulated expressions of repair factors, such as PDGF-BB, VEGF, and BMP-2, were observed at the defect area implanted with 26SCS/GelMA scaffold. This could be attributed to the electronegativity of 26SCS which facilitated the adsorption of growth factors, resulting in their longer residence time at the defect area. In addition, PDGF-BB has been reported to have the heparin-binding domain (HBD) in its structure [52–54] and it could bind to and physically interact with GAGs [55–57], which theoretically enables it to strongly bind to the heparin-like 26SCS apart from the electrostatic interactions. This assumption was confirmed by QCM curves which exhibited evident binding of 26SCS with PDGF-BB (Fig. 4C).

Cell proliferation assay showed that 26SCS could amplify the regulation effect of PDGF-BB on PSC proliferation, while this effect was not obvious with VEGF, BMP-2, FGF-2, or TGF-β1. In addition, the EdU positive rate reached the peak when the stoichiometric ratio of 26SCS: PDGF-BB was 2:1. Autodock simulation also showed that 26SCS could bind to PDGF-BB with a 2:1 stoichiometry. Notably, 26SCS-PDGF-BB complex exhibited a strengthened binding to PDGFRβ, compared with

PDGF-BB alone. According to the autodock simulation, there are interactions including hydrogen bonds and salt bridges not only between 26SCS and PDGF-BB but also between 26SCS and PDGFRβ, which makes 26SCS seem like an adhesive between PDGF-BB and PDGFRβ. The more 'flattened' conformation of PDGF-BB upon 26SCS binding might also attribute to its easier binding to PDGFRβ. In addition, the 26SCS-PDGF-BB-PDGFRβ dimer exhibited an increased stability in the fluorescence dye-based thermal shift assay, which possibly explained the more phosphorylated PDGFRβ in western blot assay. Based on these results, we inferred that 26SCS amplified the biological effect of PDGF-BB by strengthening the binding and dimerization of PDGF-BB-PDGFRβ complex, thus inducing significantly more PDGFRβ phosphorylation. According to Christa Maes et al., activation of skeletal stem and progenitor cells for bone regeneration is driven by PDGFRβ signaling [58]. Our work here confirmed improved PSC proliferation and osteogenic differentiation under the synergistic effect of 26SCS with PDGF-BB via enhanced PDGFRβ signaling. For *in vivo* bone defect repair, 26SCS could bind to endogenous PDGF-BB and amplified its regulatory effect on PSC behavior, thus promoting new bone formation.

Meaningfully, in osteoporotic mouse bone marrow where PDGF-BB concentration was significantly lower than in sham mice [45], such biological effect of 26SCS is particularly important and advantageous. Our results confirmed enriched PSC population and accelerated new bone formation at the defect after 26SCS treatment in OVX-induced osteoporotic mice, which inspired us to do further research on 26SCS in more age-related bone diseases. Further understanding of whether PSCs undergo cellular and molecular changes during aging and which regulatory mechanisms control age-associated PSC changes promises new medical approaches to degenerative bone diseases and defects. However, there were still some potential limitations in this study. Bone repair is a process involving multiple cells and factors. This study has focused on the role of PSCs in this process and has not discussed more about other cells, such as MSCs, endothelial cells, osteoclasts, etc. Besides, our results have not been verified in a natural aging induced osteoporosis model yet. Based on our findings, the future research could pay more attention to the regenerative potential of periosteum and periosteum-derived cells and develop periosteum-based new strategies and materials for bone repair.

4. Conclusion

In summary, a GelMA hydrogel scaffold loaded with 26SCS was prepared and implanted into the defect of mouse femur. The released 26SCS could effectively increase the accumulation of endogenous PDGF-BB and recruit PSCs to the defect area. In addition, 26SCS amplified the biological effect of PDGF-BB on promoting PSC proliferation and osteogenic differentiation through strengthened PDGF-BB-PDGFRβ dimer. The differentiated periosteal osteoblasts secreted more periostin by PDGF-BB, altogether providing a favorable osteogenic environment for *in situ* bone repair (Fig. 8). Our study provided a material-based PSC-involved strategy for *in situ* bone tissue engineering and potential application in age-related bone diseases.

5. Experimental section

5.1. Materials

Gelatin from porcine skin, 2-butanone, lipopolysaccharide (LPS) and 1-(4, 5-dimethylthiazol-2-yl)-3, 5-diphenylformazan (MTT) were purchased from Sigma (St. Louis, MO, USA). TRIzol reagent, PrimeScript RT reagent kit, and SYBR Premix Ex Taq were purchased from Takara Biotechnology Co. Ltd. (Dalian, China). 26SCS was synthesized as previously described [26]. All cell culture-related reagents were available from Gibco (Grand Island, NY, USA).
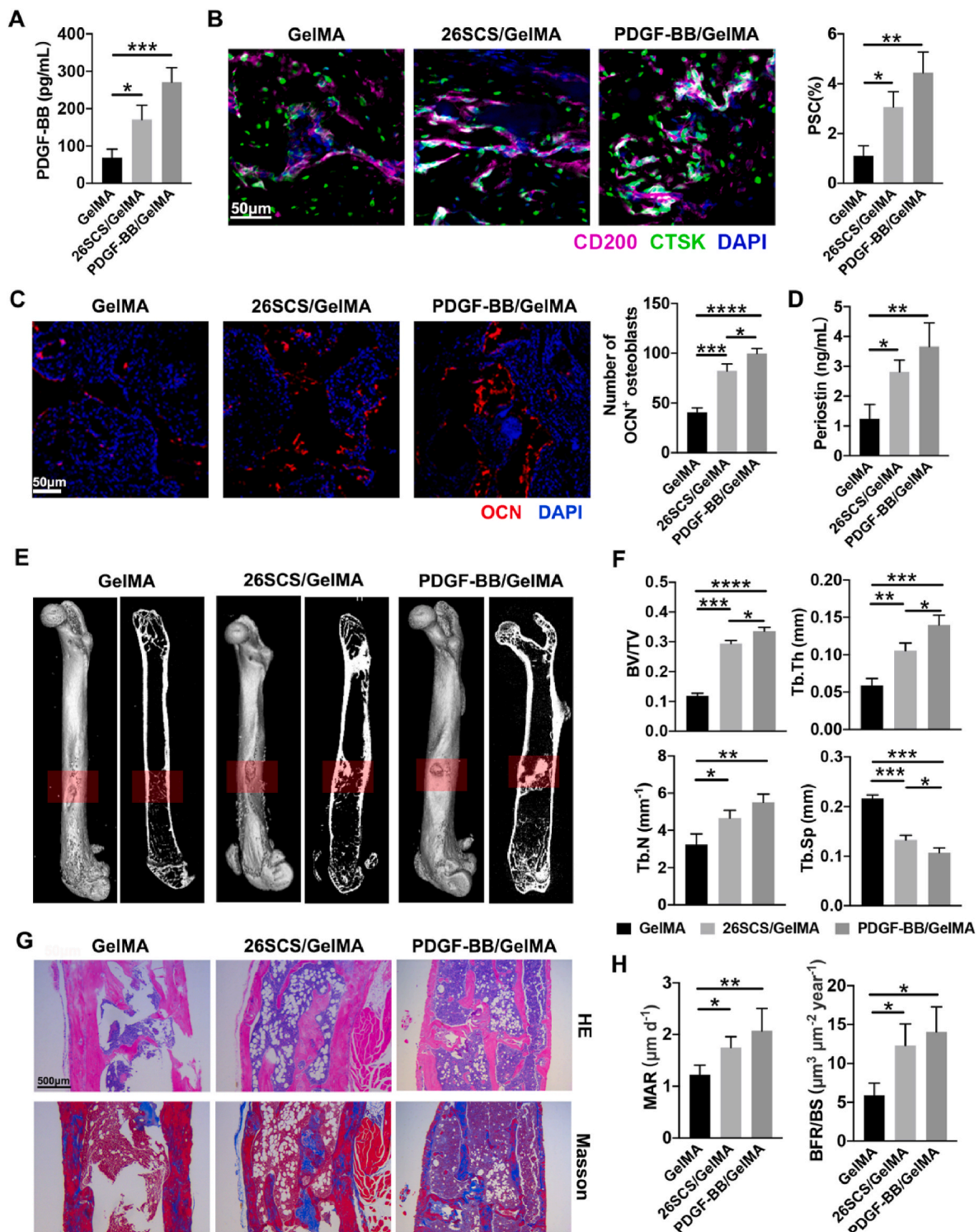
Fig. 7. 26SCS promotes PSC accumulation and new bone formation at the defect area of OVX-induced mouse osteoporotic bone. (A) PDGF-BB concentration at the defect area of OVX mice by ELISA at week 2 post-surgery. (B) Representative confocal images of immunostaining of CD200 (purple), and CTSK (green) and DAPI (blue) staining of nuclei, and quantitative analysis of the number of CD200$^+$CTSK$^+$ periosteal stem cells in the defect area of OVX mouse femora at week 2 post-surgery. (C) Representative confocal images of immunostaining of OCN (red) and DAPI (blue), and quantitative analysis of OCN$^+$ osteoblasts at the defect area of OVX mice at week 4 post-surgery. (D) Periostin concentration at the defect area of OVX mice by ELISA at week 4 post-surgery. (E) Representative micro-CT images of OVX mouse femora respectively implanted with GelMA scaffold, 26SCS/GelMA scaffold, and PDGF-BB/GelMA scaffold at week 8 post-surgery. (F) Quantitative measurements of trabecular bone fraction (BV/TV), trabecular thickness (Tb. Th), trabecular number (Tb. N), and trabecular separation (Tb. Sp). (G) Representative images of H&E staining and Masson staining of OVX mouse femora from GelMA, 26SCS/GelMA and PDGF-BB/GelMA groups respectively. (H) Quantification of mineral apposition rate (MAR) and bone formation rate (BFR) of defect area. Data shown as mean ± s.d. *$P < 0.05$, **$P < 0.01$, ***$P < 0.001$, ****$P < 0.0001$ ($n = 3$ per group).
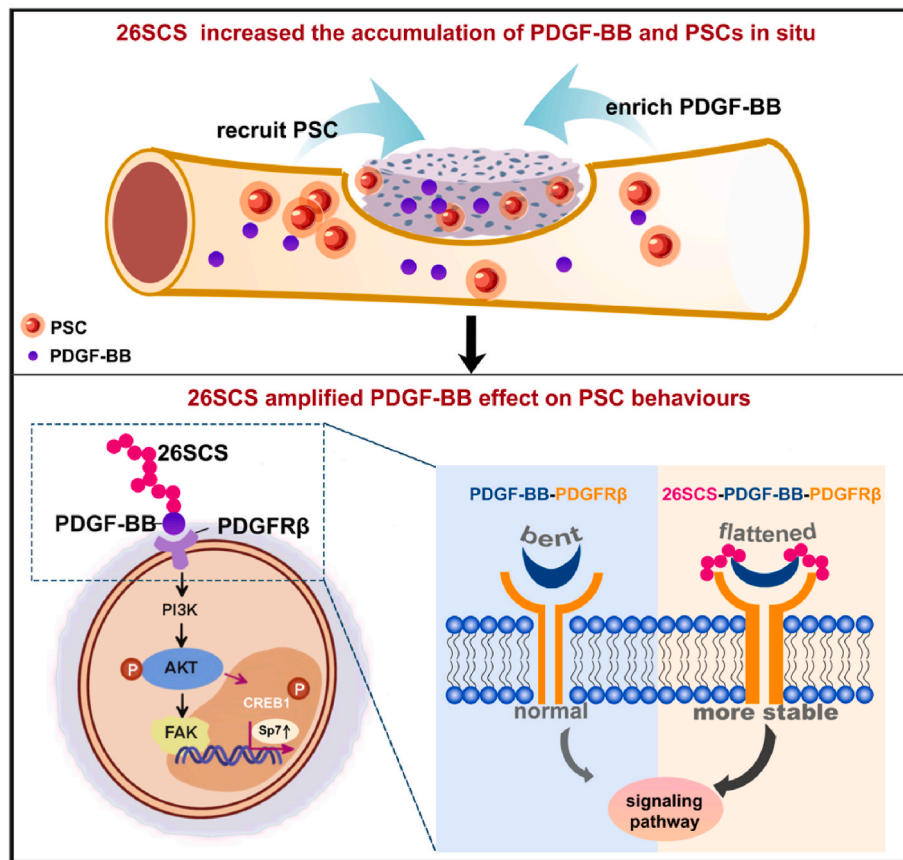
Fig. 8. Illustration of 26SCS to promote PSC-mediated *in situ* bone defect repair. First, released 26SCS from the scaffold increased the accumulation of endogenous PDGF-BB and recruited PSCs to the defect area. Subsequently, 26SCS amplified the biological effect of PDGF-BB through strengthened PDGF-BB-PDGFRβ dimer. The upregulated PDGFRβ-PI3K-Akt signaling promoted PSC proliferation and osteogenic differentiation, which realized effective *in situ* bone regeneration at the defect site.

5.2. GelMA and 26SCS/GelMA hydrogel fabrication and characterization

We prepared GelMA scaffolds for *in vivo* bone repair experiments. First, GelMA and initiator LAP were synthesized as previously described. The hydrogel scaffolds were fabricated via freeze-drying method. Briefly, GelMA was dissolved in phosphate buffer solution (PBS) at the concentrations of 5 % (w/v, 50 mg/mL), 10 % (w/v, 100 mg/mL) and 15 % (w/v, 150 mg/mL) respectively. LAP of certain concentration was added into GelMA solution with the final concentration of 0.05 % (w/v, 0.5 mg/mL) away from light. 40 μL of the mixture was put into teflon mold and the crosslinking was initiated with UV light to form GelMA hydrogel, after which the hydrogel was freeze-dried for two days to obtain GelMA scaffold. Similarly, 26SCS solution was added into GelMA solution with the final concentration of 0.025 % (w/v, 0.25 mg/mL), followed by the addition of LAP away from light. The mixed solution was crosslinked with UV light and freeze-dried for two days to obtain 26SCS/GelMA scaffold.

For mechanical property test, un-lyophilized samples were measured at a compression rate of 5 mm/min until broken. Young's modulus was obtained from the partial linear regression of the stress-strain curves. For FTIR characterization, GelMA and 26SCS/GelMA scaffolds were then analyzed in an ATR mode (Nicolet is50, Thermo, USA). For *in vivo* biocompatibility characterization, GelMA and 26SCS GelMA scaffolds were subcutaneously embedded into the back skin of C57BL/6 mice. After 14 days, mice were euthanized, and the scaffolds were isolated for immunohistochemical analysis.

5.3. The establishment of mouse femur bone defect model

Male C57BL/6 mice were purchased from Shanghai jiesijie experimental animal Co., Ltd, China. All the surgical procedures were supervised by the Animal Research Committee of East China University of Science and Technology. After the mice were anesthetized by intraperitoneal injection with pentobarbital (Nembutal, 3 mg/100g), an about 1.5 cm incision was created, and the muscles were separated carefully to expose femur. A critical-sized defect (1.2 mm in diameter and 2 mm in depth) was made by trephine bur (RWD, China), and the scaffold was implanted into the drilled defect, after which the wound was sutured and disinfected. During the surgery, forty-eight mice were randomly divided into two groups and respectively implanted with GelMA or 26SCS/GelMA scaffolds. The mice were sacrificed, and tissue samples were collected at 2, 4, and 8 weeks after operation.

5.4. Micro-CT analysis

At 8 weeks post-surgery, mouse femurs were harvested and fixed in 4 % paraformaldehyde. The samples were examined with Micro-CT (Sky scan 1076, Bruker, Germany). VG Studio software (Volume Graphics, Germany) and its auxiliary software (Scanco Medical AG, Switzerland) were employed respectively for 3D reconstruction and quantifications of new bone in the defect area.

5.5. Histological analysis

Samples were decalcified in 15 % ethylene diamine tetraacetic acid (EDTA) for 3 days with daily change of EDTA, after which they were

dehydrated in a series of ethanol and xylene and embedded in paraffin. Sections with a thickness of 4.5 μm were cut and subjected to H&E and Masson staining for the evaluation of newly formed bone, and TRAP staining for the evaluation of osteoclastogenesis. The pictures were captured by light inverted microscope (Dmi8, Leica, Germany).

5.6. Immunofluorescence staining analysis

Fresh samples were fixed in ice-cold 4 % paraformaldehyde solution at 4 °C for 4 h, decalcified in 15 % EDTA for 3 days, after which they were immersed into 20 % sucrose with 2 % polyvinylpyrrolidone (PVP) overnight at 4 °C. The samples were then embedded in OCT compound (Leica, Germany) and cut into sections with a thickness of 7 μm. Immunofluorescence staining and analysis were performed as described previously [59]. Briefly, sections were treated with 0.3 % Triton X-100 for 20 min and blocked with 5 % goat serum (Thermol Scientific, USA) at room temperature for 1 h, followed by incubation overnight at 4 °C with primary antibodies CD200, CTSK, Osterix, PDGF-BB, Periostin, OCN, CD31, EMCN, and α-SMA. Primary antibodies were then visualized by incubation of species-appropriate secondary antibodies for 1h at room temperature, and the sections were mounted by anti-fade compound with DAPI (Cell signaling technology, USA). The fluorescence images were collected by Nikon confocal microscope (A1R, Japan).

To examine dynamic bone formation, we subcutaneously injected 0.1 % calcein (Sigma, 10 mg kg^{-1} b.w.) in PBS into the mice 10 and 3 days respectively before sacrifice. Calcein double labeling was observed under a fluorescence microscope, the area between which was defined as newly formed bone during this 7-day period.

For immunofluorescence cell staining, cells were fixed with 4 % paraformaldehyde for 10 min, permeated with 0.5 % Triton-X 100 for 10 min, and blocked with 5 % goat serum for 1 h, followed by incubation overnight at 4 °C with rabbit anti-mouse primary antibody to PDGFRβ (1:100, Cell Signaling Technology). After washing with PBS twice, Alexa Fluor 700-conjugated goat anti-rabbit secondary antibody was applied to the cells for 1 h at room temperature, followed by counterstaining with Rhodamine-conjugated phalloidin (1:50, Thermo Scientific, USA) and DAPI (1:20, Thermol Scientific, USA). The fluorescence images were collected by Nikon confocal microscope (A1R, Japan).

5.7. Isolation and culture of mouse PSCs

Femurs from 4-week-old mice were collected and the periosteum was stripped and subjected to enzymatic digestion at 37 °C for 1h. The digestion buffer contained 3 mg/mL type I collagenase (Worthington), 4 mg/mL dispase (Roche Diagnostics) and 1 U/mL DNAse I (Sigma) in 1 × HBSS with calcium and magnesium. The digested tissue was transferred into staining buffer (HBSS+2 % fetal bovine serum) with 2 mM EDTA to stop the digestion, followed by centrifugation (1,000g for 5 min) to collect the periosteal cells. The cells were cultured with α-MEM (Gibco) containing 20 % fetal bovine serum (FBS, Thermo Fisher Scientific, USA), 1 % penicillin/streptomycin (Invitrogen), and 10 μM ROCK inhibitor (Y-27632, TOCRIS) in a humidified atmosphere at 37 °C, 5 % CO$_2$. On day 2, the cells were washed twice with PBS to remove non-adherent cells. At days 7–10, the cells were trypsinized and subcultured after reaching 80–90 % confluence, as passage 1. Cells of passage 3–5 were used for further experiments.

5.8. Flow cytometry analysis

The isolated PSCs were identified using flow cytometry. Briefly, the cells were trypsinized and collected into a tube. After centrifugation at 300g for 5 min, the supernatant was removed and the cells at the bottom were resuspended with 100 μL staining buffer. Under the light proof condition, the cells were stained with BV420-conjugated CD31, PE-conjugated CD45, APC-conjugated CD200 and PE/Cy7-conjugated CD105 at 4 °C for 30 min. The cell suspension was then assessed on

Cytoflex LX (Beckman coulter, USA) and the data were analyzed using FlowJo Software.

Flow cytometry was also employed to investigate *in vivo* cell recruitment in the defect area. Briefly, the samples were collected and ground with agate mortar with 1 mL PBS. After centrifugation at 300g for 10 min, the supernatants were collected and stored at −80 °C for further analysis. The tissues at the bottom were enzymatically digested with 3 mg/ml collagenase type I (Gibco) and 4 mg/ml neutral protease (Roche) for 15 min at 37 °C to obtain a single cell suspension. The cell suspension was then filtered (40 μm) and washed with staining buffer. Under the light proof condition, the cells were stained with BV420-conjugated CD31, PE-conjugated CD45, PE-conjugated Ter119, APC-conjugated CD200 and PE/Cy7-conjugated CD105 at 4 °C for 45min. The cell suspension was then assessed on Cytoflex LX (Beckman coulter, USA) and the data were analyzed using FlowJo Software.

5.9. Enzyme-linked immunosorbent assay (ELISA) analysis

PDGF-BB, VEGF, TGF-β1, FGF2, and BMP2 Quantikine ELISA kits (NeoBioscience) were used according to the manufacturer's instructions to determine the levels in the implant supernatant mentioned above. The total protein concentration was measured using BCA Protein Assay Kit (Beyotime, China) to normalize the expression of factors.

5.10. EdU cell proliferation assay

EdU cell proliferation assay was conducted to evaluate the proliferation of cells according to the manufacturer's instructions. PSCs were seeded in 12-well plates at the density of 1×10^5 cells/well and cultured with 26SCS and growth factors for 24 h before the assay. A total of 500 μL EdU (10 μM) reagent (Beyotime, China) was added to each well. After 2 h of incubation, cells were washed for three times with PBS, fixed with 4 % paraformaldehyde solution for 15 min, permeabilized with 0.3 % Triton X-100 for another 15 min, and then incubated with the click-reaction reagent for 30 min at room temperature away from light. The nucleus was counterstained with DAPI (1:20, Thermol Scientific, USA). The fluorescence images were collected by Nikon confocal microscope (A1R, Japan).

5.11. MTT assay

PSCs were seeded at a density of 1×10^4 cells/well in 96-well plate, and cultured overnight in α-MEM containing 20 % FBS, 1 % penicillin/streptomycin and 10 μM ROCK inhibitor at 37 °C, 5 % CO$_2$, in a humidified environment. The cells of different groups were then respectively cultured with the medium containing 2 nM 26SCS, 1 nM PDGF-BB, and 2 nM 26SCS plus 1 nM PDGF-BB. The group cultured with the medium without 26SCS or PDGF-BB served as a negative control. After cultivation for 1 day, 3 days and 7 days, MTT assay was performed according to the manufacturer's instructions. The absorbance at 490 nm was measured. All groups were detected in quintuplicate, and the results were normalized to the control group.

5.12. Cell migration assay

A scratch wound healing assay was conducted to assess the migratory capacity of PSCs under different conditions. Briefly, EGFP-PSCs were seeded at a density of 1×10^4 cells/well in 96-well plate and cultured at 37 °C, 5 % CO$_2$ until reaching 100 % confluency. Vertically linear scratches were made with a sterile pipette tip on the surface of the well, followed by washing with PBS twice gently to remove cell debris. The cells of different groups were then respectively cultured with different medium containing 2 % FBS (α-MEM, α-MEM with 2 nM 26SCS, α-MEM with 1 nM PDGF-BB, and α-MEM with 2 nM 26SCS plus 1 nM PDGF-BB). Images of cells were captured at 0 h and 12 h post-scratching with Nikon confocal microscope. The repaired area was quantified with ImageJ

software (n = 5).

5.13. Western blot analysis

PSCs were seeded at a density of 2×10^5 cells/well in 6-well plate and cultured in α-MEM containing 20 % FBS, 1 % penicillin/streptomycin and 10 μM ROCK inhibitor at 37 °C, 5 % CO_2, in a humidified environment. After reaching 100 % confluency, the cells were treated with starvation culture overnight in the medium containing 2 % FBS, followed by stimulation with 2 nM 26SCS, 1 nM PDGF-BB, and 2 nM 26SCS plus 1 nM PDGF-BB respectively for 15 min. The group without 26SCS or PDGF-BB treatment served as a negative control. The cells were then lysed by cold radioimmuno-precipitation assay (RIPA) buffer with 1 mM phenylmethanesulfonyl fluoride (PMSF) for 10 min to obtain the total protein. The cell lysates were collected and equilibrated with loading buffer to an equal concentration, and then boiled for 10 min to obtain stabilized protein. Subsequently, the protein was separated by 8 % SDS-PAGE at an equal concentration, and then blotted onto nitrocellulose membranes (Merck, USA). After blocking with 5 % BSA, the membranes were incubated with specific primary antibodies against PDGFRβ (1:1000, Cell Signaling Technology, USA) and p-PDGFRβ (1:1000, Cell Signaling Technology, USA) at 4 °C overnight, followed by incubation with corresponding HRP-conjugated secondary antibodies (1:1000, Cell Signaling Technology, USA) at room temperature for 2 h. GAPDH was used as a loading control. Visualization of the protein bands was performed with a chemiluminescence imaging system (Tanon, Shanghai, China). Total intensity of each band was determined with Tanon Image software (version 1.10; Tanon, Shanghai, China).

5.14. Quartz crystal microbalance (QCM) experiment

QCM (Q-Sence AB, Sweden) analysis was conducted to detect the bonding effect between PDGF-BB and PDGFRβ. Briefly, Au chips (Φ = 14 mm, 5 MHz) were immersed into 1 mM 11-AUT solution in ethanol at room temperature for 12 h to introduce amine groups onto the surface, rinsed with alcohol and purified water, and finally dried with nitrogen for subsequent use. PBS first flowed through chip chambers to establish a stable baseline, followed by 50 μg/mL PDGF-BB. After the curve approaches to flatness, PBS was perfused again into chambers to wash off the unbound protein, followed by the flow of 5 % BSA to block nonspecific bonding. 50 μg/mL PDGFRβ was then injected into chambers until reaching stability. To explore the effect of 26SCS on the affinity between PDGF-BB and PDGFRβ, 0.5 mg/mL 26SCS was first pumped into chambers after the establishment of the baseline with PBS, followed by the sequential injection of PBS, 50 μg/mL PDGF-BB, PBS, 5 % BSA, 50 μg/mL PDGFRβ and finally PBS. All experiments were performed at a constant flow rate of 25 μL/min. It should be mentioned that after each injection, the curve must return to flatness before the next.

The relative value (v1) of PDGFRβ binding to PDGF-BB was obtained by the equation $v1 = \frac{\Delta f_{PDGFR\beta}}{\Delta f_{PDGF-BB}}$

And the relative value (v2) of PDGFRβ binding to PDGF-BB after PDGF-BB was bound to 26SCS was obtained by the equation $v2 = \frac{\Delta f'_{PDGFR\beta}}{\Delta f'_{PDGF-BB}}$

Where Δf and Δf' represent the shift of frequency without or with the effect of 26SCS respectively.

5.15. Quantitative real-time PCR (qRT-PCR) analysis

To investigate gene expression in PSCs stimulated by SCS with PDGF-BB, qRT-PCR was performed. PSCs were seeded in 6-well plates and treated with 2 nM 26SCS, 1 nM PDGF-BB, and 2 nM 26SCS plus 1 nM PDGF-BB respectively. The group without 26SCS or PDGF-BB treatment was set as a negative control. After 12 h, total RNAs were extracted with TRIzol reagent, followed by a reverse transcription step with Prime-Script RT reagent kit according to the manufacturer's instructions. The

qRT-PCR was performed on a CFX96 Touch PCR detection system (Bio-Rad, USA) with a hot start denaturation step at 95 °C for 30 s, and then fluorescence intensity was recorded during 40 cycles at 95 °C for 5 s and 60 °C for 30 s. GAPDH was used as a housekeeping gene to normalize the expression of the gene of interest depending on the experiment. The sequences of primers are listed in Table S1.

5.16. Autodock simulation

MOE 2020.0901 software was used for autodock simulation. The complex of PDGF-BB (PDB-ID: 4QCI) and 26SCS (20 units) was first constructed using MOE DOCK module. A ternary complex of above structure (26SCS/PDGF-BB) and PDGFRβ (PDB-ID: 3MJG) was then constructed using Protein-Protein module. The binding energy was calculated through MOE DOCK and MMGBVI. PDGF-BB structures in different status were aligned and the displacements including the twist angle and bending distance were calculated.

5.17. Fluorescence dye-based thermal shift assay

Thermal stability assays were performed with a real-time PCR system (Bio-Rad). The SYPRO Orange dye (ThermoFisher Scientific) was used as a fluorescent probe (diluted to 50 × from a 5000 × stock solution). 10 μL of protein solution (1 mg/mL), 2.5 μL of 50 × SYPRO stock solution, and 12.5 μL of Tris buffer solution (150 mM NaCl) were successively added into each well of a 96-well plate. The temperature gradient was carried out in the range of 10°C–95 °C at 0.5 °C/10s. Fluorescence was recorded as a function of temperature in real time. The melting temperature (Tm) was calculated as the maximum of the derivative of the resulting SYPRO Orange fluorescence curves.

5.18. Multi-differentiation experiments of PSCs

For osteogenic differentiation, PSCs were seeded at the density of 2×10^5 cells/well in 6-well plates pre-coated with 0.1 % gelatin solution and cultured at 37 °C, 5 % CO_2, in a humidified environment. After reaching 60–70 % confluency, the medium was replaced with osteogenic differentiation medium (C57BL/6 Mouse Mesenchymal Stem Cell Osteogenic Differentiation kit, MUBMX-90021) containing 2 nM 26SCS, 1 nM PDGF-BB, and 2 nM 26SCS plus 1 nM PDGF-BB respectively. Medium was changed every 3 days for 14–20 days. At the end of this period, cells were washed with PBS and fixed with 4 % paraformaldehyde solution for 30 min. After that, cells were washed with PBS twice and stained with alizarin red solution for 3–5 min. Cells were then washed with PBS twice and air dried before microscopic visualization.

For adipogenic differentiation, PSCs were seeded at the density of 2×10^5 cells/well in 6-well plates and cultured at 37 °C, 5 % CO_2, in a humidified environment. Medium was changed every 3 days until reaching 100 % confluency. Cells were then allowed to differentiate in adipogenic differentiation medium (C57BL/6 Mouse Mesenchymal Stem Cell Adipogenic Differentiation kit, MUBMX-90031) containing 2 nM 26SCS, 1 nM PDGF-BB, and 2 nM 26SCS plus 1 nM PDGF-BB respectively. Medium was changed every 3 days for a total of 14–20 days until the appearance of large round lipid droplets. The medium was then removed, and cells were washed with PBS and fixed with 4 % paraformaldehyde solution for 30 min. Cells were rinsed again with PBS twice and stained with oil red O working solution (3:2 dilution with water) for 30 min. Cells were washed with PBS twice for the observation under a light microscope.

For chondrogenic differentiation, $3-4 \times 10^5$ cells were seeded in a 15-mL centrifuge tube. After centrifugation at 250g for 4 min, the supernatant was removed and chondrogenic differentiation medium (C57BL/6 Mouse Mesenchymal Stem Cell Chondrogenic Differentiation kit, MUBMX-90041) containing 2 nM 26SCS, 1 nM PDGF-BB, and 2 nM 26SCS plus 1 nM PDGF-BB respectively was slowly added. Cells were incubated at 37 °C, 5 % CO_2, in a humidified environment. Fresh

medium was added every 2–3 days. After a period of 21–28 days, the pellet was fixed with 4 % paraformaldehyde solution for 30 min and embedded in paraffin. Sections with a thickness of 4.5 μm were cut and stained with alcian blue solution for 30 min for the observation under a light microscope.

5.19. Statistical analysis

All data were shown as mean ± SD. Results were analyzed using one-way ANOVA in GraphPad PRISM software (version 8.0; GraphPad, La Jolla, CA, USA). A p value < 0.05 was considered statistically significant: $*P < 0.05$; $**P < 0.01$; $***P < 0.001$; $****P < 0.0001$.

Declaration of competing interest

The authors declare no conflict of interest.

Ethics approval and consent to participate

All the surgical procedures were supervised by the Animal Research Committee of East China University of Science and Technology. The ethic number is ECUST-21010.

CRediT authorship contribution statement

Luli Ji: Conceptualization, Data curation, Formal analysis, Visualization, Writing – original draft. **Yuanman Yu:** Methodology. **Fuwei Zhu:** Data curation. **Dongao Huang:** Data curation. **Xiaogang Wang:** Conceptualization, Data curation, Writing – review & editing. **Jing Wang:** Project administration, Supervision, Writing – review & editing. **Changsheng Liu:** Funding acquisition, Project administration.

Acknowledgements

Appendix A. Supplementary data

Supplementary data to this article can be found online at https://doi.org/10.1016/j.bioactmat.2023.12.016.

References

[1] R. Langer, J. Vacanti, Tissue engineering, Science 260 (5110) (1993), 1993.
[2] H. Feng, B. Jiang, W. Xing, J. Sun, M.B. Greenblatt, W. Zou, Skeletal Stem Cells: Origins, definitions, and functions in bone development and disease, Life Med. 1 (3) (2022) 276–293.
[3] B. Huang, P. Li, M. Chen, L. Peng, X. Luo, G. Tian, H. Wang, L. Wu, Q. Tian, H. Li, Hydrogel composite scaffolds achieve recruitment and chondrogenesis in cartilage tissue engineering applications, J. Nanobiotechnol. 20 (1) (2022) 25.
[4] K. Takahashi, S. Yamanaka, Induction of pluripotent stem cells from mouse embryonic and adult fibroblast cultures by defined factors, Cell 126 (4) (2006) 663–676.
[5] M. Lutolf, J. Hubbell, Synthetic biomaterials as instructive extracellular microenvironments for morphogenesis in tissue engineering, Nat. Biotechnol. 23 (1) (2005) 47–55.
[6] A.K. Gaharwar, I. Singh, A. Khademhosseini, Engineered biomaterials for in situ tissue regeneration, Nat. Rev. Mater. 5 (9) (2020) 686–705.
[7] E.R. Ruskowitz, C.A. DeForest, Photoresponsive biomaterials for targeted drug delivery and 4D cell culture, Nat. Rev. Mater. 3 (2) (2018) 1–17.
[8] M.R. Allen, J.M. Hock, D.B. Burr, Periosteum: biology, regulation, and response to osteoporosis therapies, Bone 35 (5) (2004) 1003–1012.
[9] K.N. Malizos, L.K. Papatheodorou, The healing potential of the periosteum: molecular aspects, Injury 36 (3) (2005) S13–S19.
[10] S.J. Roberts, N. Van Gastel, G. Carmeliet, F.P. Luyten, Uncovering the periosteum for skeletal regeneration: the stem cell that lies beneath, Bone 70 (2015) 10–18.
[11] S. Debnath, A.R. Yallowitz, J. McCormick, S. Lalani, T. Zhang, R. Xu, N. Li, Y. Liu, Y.S. Yang, M. Eiseman, Discovery of a periosteal stem cell mediating intramembranous bone formation, Nature 562 (7725) (2018) 133–139.
[12] J. Xu, Y. Wang, Z. Li, Y. Tian, Z. Li, A. Lu, C.-Y. Hsu, S. Negri, C. Tang, R.J. Tower, PDGFRα reporter activity identifies periosteal progenitor cells critical for bone formation and fracture repair, Bone Res. 10 (1) (2022) 1–15.
[13] O.D. de Lageneste, A. Julien, R. Abou-Khalil, G. Frangi, C. Carvalho, N. Cagnard, C. Cordier, S.J. Conway, C. Colnot, Periosteum contains skeletal stem cells with high bone regenerative potential controlled by Periostin, Nat. Commun. 9 (1) (2018) 1–15.
[14] M. Tsukasaki, N. Komatsu, T. Negishi-Koga, N.C.-N. Huynh, R. Muro, Y. Ando, Y. Seki, A. Terashima, W. Pluemsakunthai, T. Nitta, Periosteal stem cells control growth plate stem cells during postnatal skeletal growth, Nat. Commun. 13 (1) (2022) 1–11.
[15] S. Bok, A.R. Yallowitz, J. Sun, J. McCormick, M. Cung, L. Hu, S. Lalani, Z. Li, B. R. Sosa, T. Baumgartner, A multi-stem cell basis for craniosynostosis and calvarial mineralization, Nature (2023) 1–9.
[16] X. Zhao, S. Liu, L. Yildirimer, H. Zhao, R. Ding, H. Wang, W. Cui, D. Weitz, Injectable stem cell-laden photocrosslinkable microspheres fabricated using microfluidics for rapid generation of osteogenic tissue constructs, Adv. Funct. Mater. 26 (17) (2016) 2809–2819.
[17] S. Shen, R. Liu, C. Song, T. Shen, Y. Zhou, J. Guo, B. Kong, Q. Jiang, Fish scale-derived scaffolds with MSCs loading for photothermal therapy of bone defect, Nano Res. (2023) 1–10.
[18] J. Bolander, Y.C. Chai, L. Geris, J. Schrooten, D. Lambrechts, S.J. Roberts, F. P. Luyten, Early BMP, Wnt and Ca2+/PKC pathway activation predicts the bone forming capacity of periosteal cells in combination with calcium phosphates, Biomaterials 86 (2016) 106–118.
[19] S.F. Evans, D. Docheva, A. Bernecker, C. Colnot, R.P. Richter, M.L.K. Tate, Solid-supported lipid bilayers to drive stem cell fate and tissue architecture using periosteum derived progenitor cells, Biomaterials 34 (8) (2013) 1878–1887.
[20] J.-H. Lee, J.-H. Kim, S.-H. Oh, S.-J. Kim, Y.-S. Hah, B.-W. Park, D.R. Kim, G.-J. Rho, G.-H. Maeng, R.-H. Jeon, Tissue-engineered bone formation using periosteal-derived cells and polydioxanone/pluronic F127 scaffold with pre-seeded adipose tissue-derived CD146 positive endothelial-like cells, Biomaterials 32 (22) (2011) 5033–5045.
[21] K. Yukata, C. Xie, T.-F. Li, M. Takahata, D. Hoak, S. Kondabolu, X. Zhang, H. A. Awad, E.M. Schwarz, C.A. Beck, Aging periosteal progenitor cells have reduced regenerative responsiveness to bone injury and to the anabolic actions of PTH 1-34 treatment, Bone 62 (2014) 79–89.
[22] S. Morla, Glycosaminoglycans and glycosaminoglycan mimetics in cancer and inflammation, Int. J. Mol. Sci. 20 (8) (2019) 1963.
[23] R.L. Jackson, S.J. Busch, A.D. Cardin, Glycosaminoglycans: molecular properties, protein interactions, and role in physiological processes, Physiol. Rev. 71 (2) (1991) 481–539.
[24] M. Wang, X. Liu, Z. Lyu, H. Gu, D. Li, H. Chen, Glycosaminoglycans (GAGs) and GAG mimetics regulate the behavior of stem cell differentiation, Colloids Surf. B Biointerfaces 150 (2017) 175–182.
[25] S. Samantray, O.O. Olubiyi, B. Strodel, The Influences of sulphation, salt type, and salt concentration on the structural heterogeneity of glycosaminoglycans, Int. J. Mol. Sci. 22 (21) (2021) 11529.
[26] H. Chen, Y. Yu, C. Wang, J. Wang, C. Liu, The regulatory role of sulfated polysaccharides in facilitating rhBMP-2-induced osteogenesis, Biomater. Sci. 7 (10) (2019) 4375–4387.
[27] B. Kong, Y. Chen, R. Liu, X. Liu, C. Liu, Z. Shao, L. Xiong, X. Liu, W. Sun, S. Mi, Fiber reinforced GelMA hydrogel to induce the regeneration of corneal stroma, Nat. Commun. 11 (1) (2020) 1435.
[28] N. Bonnet, J. Brun, J.C. Rousseau, L.T. Duong, S.L. Ferrari, Cathepsin K controls cortical bone formation by degrading periostin, J. Bone Miner. Res. 32 (7) (2017) 1432–1441.
[29] T.G. Kashima, T. Nishiyama, K. Shimazu, M. Shimazaki, I. Kii, A.E. Grigoriadis, M. Fukayama, A. Kudo, Periostin, a novel marker of intramembranous ossification, is expressed in fibrous dysplasia and in c-Fos–overexpressing bone lesions, Hum. Pathol. 40 (2) (2009) 226–237.
[30] N. Bonnet, S.J. Conway, S.L. Ferrari, Regulation of beta catenin signaling and parathyroid hormone anabolic effects in bone by the matricellular protein periostin, Proc. Natl. Acad. Sci. USA 109 (37) (2012) 15048–15053.
[31] R. Marsell, T.A. Einhorn, The biology of fracture healing, Injury 42 (6) (2011) 551–555.
[32] R. Chung, B.K. Foster, C.J. Xian, Injury responses and repair mechanisms of the injured growth plate, Front. Biosci. 3 (2011) 117–125.
[33] B. Gao, R. Deng, Y. Chai, H. Chen, B. Hu, X. Wang, S. Zhu, Y. Cao, S. Ni, M. Wan, Macrophage-lineage TRAP+ cells recruit periosteum-derived cells for periosteal osteogenesis and regeneration, J. Clin. Invest. 129 (6) (2019) 2578–2594.
[34] A.P. Kusumbe, S.K. Ramasamy, R.H. Adams, Coupling of angiogenesis and osteogenesis by a specific vessel subtype in bone, Nature 507 (7492) (2014) 323–328.
[35] X. Wang, B.G. Matthews, J. Yu, S. Novak, D. Grcevic, A. Sanjay, I. Kalajzic, PDGF modulates BMP2-induced osteogenesis in periosteal progenitor cells, JBMR plus 3 (5) (2019) e10127.
[36] H. Chen, C.-F. Xu, J. Ma, A.V. Eliseenkova, W. Li, P.M. Pollock, N. Pitteloud, W. T. Miller, T.A. Neubert, M. Mohammadi, A crystallographic snapshot of tyrosine trans-phosphorylation in action, Proc. Natl. Acad. Sci. USA 105 (50) (2008) 19660–19665.
[37] R. Goetz, M. Mohammadi, Exploring mechanisms of FGF signalling through the lens of structural biology, Nat. Rev. Mol. Cell Biol. 14 (3) (2013) 166–180.
[38] S.R. Hubbard, Juxtamembrane autoinhibition in receptor tyrosine kinases, Nat. Rev. Mol. Cell Biol. 5 (6) (2004) 464–471.

[39] T. Hunter, Tyrosine phosphorylation in cell signaling and disease, Keio J. Med. 51 (2) (2002) 61–71.

[40] N. Jura, X. Zhang, N.F. Endres, M.A. Seeliger, T. Schindler, J. Kuriyan, Catalytic control in the EGF receptor and its connection to general kinase regulatory mechanisms, Mol. Cell 42 (1) (2011) 9–22.

[41] M.A. Lemmon, J. Schlessinger, Cell signaling by receptor tyrosine kinases, Cell 141 (7) (2010) 1117–1134.

[42] Z. Huang, W.M. Marsiglia, U.B. Roy, N. Rahimi, D. Ilghari, H. Wang, H. Chen, W. Gai, S. Blais, T.A. Neubert, Two FGF receptor kinase molecules act in concert to recruit and transphosphorylate phospholipase Cγ, Mol. Cell 61 (1) (2016) 98–110.

[43] P. Bianco, X. Cao, P.S. Frenette, J.J. Mao, P.G. Robey, P.J. Simmons, C.-Y. Wang, The meaning, the sense and the significance: translating the science of mesenchymal stem cells into medicine, Nat. Med. 19 (1) (2013) 35–42.

[44] B.O. Zhou, R. Yue, M.M. Murphy, J.G. Peyer, S.J. Morrison, Leptin-receptor-expressing mesenchymal stromal cells represent the main source of bone formed by adult bone marrow, Cell Stem Cell 15 (2) (2014) 154–168.

[45] H. Xie, Z. Cui, L. Wang, Z. Xia, Y. Hu, L. Xian, C. Li, L. Xie, J. Crane, M. Wan, PDGF-BB secreted by preosteoclasts induces angiogenesis during coupling with osteogenesis, Nat. Med. 20 (11) (2014) 1270–1278.

[46] L.C. Ortinau, H. Wang, K. Lei, L. Deveza, Y. Jeong, Y. Hara, I. Grafe, S.B. Rosenfeld, D. Lee, B. Lee, Identification of functionally distinct Mx1+ αSMA+ periosteal skeletal stem cells, Cell Stem Cell 25 (6) (2019) 784–796. e5.

[47] P. Leucht, J.-B. Kim, R. Amasha, A.W. James, S. Girod, J.A. Helms, Embryonic Origin and Hox Status Determine Progenitor Cell Fate during Adult Bone Regeneration, 2008.

[48] X. Zhang, A. Naik, C. Xie, D. Reynolds, J. Palmer, A. Lin, H. Awad, R. Guldberg, E. Schwarz, R. O Keefe, Periosteal stem cells are essential for bone revitalization and repair, J. Musculoskelet. Neuronal Interact. 5 (4) (2005) 360.

[49] Y. Koshihara, M. Hirano, M. Kawamura, H. Oda, S. Higaki, Mineralization ability of cultured human osteoblast-like periosteal cells does not decline with aging, J. Gerontol. 46 (5) (1991) B201–B206.

[50] Q. Wei, A. Holle, J. Li, F. Posa, F. Biagioni, O. Croci, A.S. Benk, J. Young, F. Noureddine, J. Deng, BMP-2 signaling and mechanotransduction synergize to drive osteogenic differentiation via YAP/TAZ, Adv. Sci. 7 (15) (2020) 1902931.

[51] J. Eyckmans, G.L. Lin, C.S. Chen, Adhesive and mechanical regulation of mesenchymal stem cell differentiation in human bone marrow and periosteum-derived progenitor cells, Biol. Open 1 (11) (2012) 1058–1068.

[52] O. Evrova, J. Buschmann, In vitro and in vivo effects of PDGF-BB delivery strategies on tendon healing: a review, Eur. Cell. Mater. 34 (2017) 15–39.

[53] S. Thomopoulos, M. Zaegel, R. Das, F.L. Harwood, M.J. Silva, D. Amiel, S. Sakiyama-Elbert, R.H. Gelberman, PDGF-BB released in tendon repair using a novel delivery system promotes cell proliferation and collagen remodeling, J. Orthop. Res. 25 (10) (2007) 1358–1368.

[54] D. Schilling, J.D. Reid IV, A. Hujer, D. Morgan, E. Demoll, P. Bummer, R. A. Fenstermaker, D.M. Kaetzel, Loop III region of platelet-derived growth factor (PDGF) B-chain mediates binding to PDGF receptors and heparin, Biochem. J. 333 (3) (1998) 637–644.

[55] G. Fager, G. Camejo, U. Olsson, G. Östergren-Lundén, F. Lustig, G. Bondjers, Binding of platelet-derived growth factor and low density lipoproteins to glycosaminoglycan species produced by human arterial smooth muscle cells, J. Cell. Physiol. 163 (2) (1995) 380–392.

[56] F. Lustig, J. Hoebeke, C. Simonson, G. Östergren-Lundén, G. Bondjers, U. Rüetchi, G. Fager, Processing of PDGF gene products determines interactions with glycosaminoglycans, J. Mol. Recogn. 12 (2) (1999) 112–120.

[57] R. García-Olivas, J. Hoebeke, S. Castel, M. Reina, G. Fager, F. Lustig, S. Vilaró, Differential binding of platelet-derived growth factor isoforms to glycosaminoglycans, Histochem. Cell Biol. 120 (5) (2003) 371–382.

[58] A.-M. Böhm, N. Dirckx, R.J. Tower, N. Peredo, S. Vanuytven, K. Theunis, E. Nefyodova, R. Cardoen, V. Lindner, T. Voet, Activation of skeletal stem and progenitor cells for bone regeneration is driven by PDGFRβ signaling, Dev. Cell 51 (2) (2019) 236–254, e12.

[59] A.P. Kusumbe, S.K. Ramasamy, A. Starsichova, R.H. Adams, Sample preparation for high-resolution 3D confocal imaging of mouse skeletal tissue, Nat. Protoc. 10 (12) (2015) 1904–1914.